



Cite this: *Soft Matter*, 2019, 15, 4751

Core-crystalline nanoribbons of controlled length via diffusion-limited colloid aggregation†

Ruth N. Schmarsow,^a Marcelo Ceolín,^b Ileana A. Zucchi^a and Walter F. Schroeder^{ib*}

It has been previously reported that poly(ethylene) (PE)-based block copolymers self-assemble in certain thermosetting matrices to form a dispersion of one-dimensional (1D) nanoribbons. Such materials exhibit exceptional properties that originate from the high aspect ratio of the elongated nano-objects. However, the ability to prepare 1D assemblies with well-controlled dimensions is limited and represents a key challenge. Here, we demonstrate that the length of ribbon-like nanostructures can be precisely controlled by regulating the mobility of the matrix during crystallization of the core-forming PE block. The selected system to prove this concept was a poly(ethylene-*block*-ethylene oxide) (PE-*b*-PEO) block copolymer in an epoxy monomer based on diglycidyl ether of bisphenol A (DGEBA). The system was activated with a dual thermal- and photo-curing system, which allowed us to initiate the epoxy polymerization at 120 °C until a certain degree of conversion, stop the reaction by cooling to induce crystallization and micellar elongation, and then continue the polymerization at room temperature by visible-light irradiation. In this way, crystallization of PE blocks took place in a matrix whose mobility was regulated by the degree of conversion reached at 120 °C. The mechanism of micellar elongation was conceptualized as a diffusion-limited colloid aggregation process which was induced by crystallization of PE cores. This assertion was supported by the evidence obtained from *in situ* small-angle X-ray scattering (SAXS), in combination with differential scanning calorimetry (DSC) and transmission electron microscopy (TEM).

Received 26th March 2019,
Accepted 21st May 2019

DOI: 10.1039/c9sm00615j

rsc.li/soft-matter-journal

Introduction

One-dimensional (1D) nanoribbons have received extensive attention in recent years due to their unique properties that originate from their high aspect ratio. Representative examples include nanoribbons based on graphene,^{1,2} black phosphorus,³ transition metal dichalcogenides,^{4,5} cellulose,⁶ and clay,^{7,8} which are promising materials for applications in electronics, photonics, catalysis, packaging and composite reinforcement. The resulting properties of these materials strongly depend on

their width, length and particle size polydispersity.⁹ Therefore, the ability to precisely control the dimensions of 1D nanoribbons is of critical technological importance for many of their applications.

The self-assembly of block-copolymers (BCP) in selective solvents is a potential route to 1D nanostructures with controlled dimensions. In this approach, selective solvation results in micellar aggregates whose morphology depends on several factors, such as length of each block, concentration, thermodynamic compatibility between block-solvent and block-block, and temperature.^{10,11} Moreover, if the insoluble core-forming block is able to crystallize, crystal packing forces play a dominant role in determining the architecture of the micellar aggregates that are formed.¹² In this way, a large variety of morphologies can be prepared by adjusting the crystallization conditions in which semicrystalline micelles are obtained. On the basis of this concept, crystallization-driven self-assembly has emerged as a powerful method for the preparation of well-defined micellar structures with controlled dimensions. For example, Winnik and Manners found that poly(ferrocenylsilane) (PFS)-based block copolymers self-assemble into cylindrical micelles^{13–15} or tape-like nanostructures¹⁶ when they are dispersed in alkane solvents. Because their ends remain active, these micelles can be elongated, in a controlled manner, through the addition of further block

^a Institute of Materials Science and Technology (INTEMA), University of Mar del Plata and National Research Council (CONICET), Juan B. Justo 4302, 7600 Mar del Plata, Argentina. E-mail: wschroeder@fi.mdp.edu.ar

^b Instituto de Investigaciones Físicoquímicas Teóricas y Aplicadas (INIFTA), Universidad Nacional de La Plata, CONICET, CC 16-Suc. 4, 1900 La Plata, Argentina

† Electronic supplementary information (ESI) available: Brief description of both polymerization mechanisms employed. SAXS profiles of the neat PE-*b*-PEO block copolymer at different temperatures. Conversion of epoxy groups vs. time for a mixture containing 10 wt% BCP using a protocol of two consecutive thermal- and photo-curing steps. TEM image of a fully photocured material ($x_t = 0$). Table containing the fitting results of SAXS data corresponding to samples obtained with different values of x_t . TOM micrographs of the unreacted sample with 10 wt% BCP at two different temperatures: 120 °C and RT. See DOI: 10.1039/c9sm00615j

copolymer unimers. It was argued that the process is driven by epitaxial crystallization of the core-forming PFS block on the preformed seed micelles.^{17,18} In other examples, analogous elongated structures with crystallizable organic cores based on poly(ethylene oxide) (PEO),¹⁹ poly(ϵ -caprolactone) (PCL),²⁰ and poly(ethylene) (PE),²¹ were prepared in a controlled way by regulating parameters such as cooling rate and crystallization temperature. While a significant number of articles describing the preparation of well-defined 1D nanostructures in solution have been published in recent years, only a few reports have addressed the formation of this kind of structures in polymer matrices.^{22–24}

Bates and co-workers, first reported the strategy of creating nanostructures in epoxy matrices through self-assembly of BCP.²⁵ In this approach, the matrix precursors act as a block-selective solvent giving place to micellar structures before curing reaction. These preformed structures are then fixed by the polymerization reaction of the matrix. The condition for this approach is that the miscible block does not phase separate during reaction in order to avoid macrophase separation. More recently, Zheng *et al.*²⁶ demonstrated that the nanostructuring of BCP in thermosetting matrices can be produced along polymerization, starting from a homogeneous solution of the BCP in the matrix precursors. Here, the condition is that one of the blocks phase separates during polymerization while the other one remains miscible throughout the reaction. In any case, the generated nanostructure can evolve during polymerization due to changes in the quality of the thermoset as a solvent of the miscible block,^{27–29} or by crystallization of the immiscible block.²⁴

At present, relatively little is known about fabrication and manipulation of BCP micelles with semicrystalline core in thermosetting matrices.^{22–24,30,31} It was found that when the curing reaction is performed below the crystallization temperature of the crystallizable core-forming block, elongated planar nanostructures dispersed in the polymer matrix can be obtained. For example, Zucchi *et al.*²² studied the nanostructuring of poly(ethylene-*block*-ethylene oxide) (PE-*b*-PEO) block copolymer dispersed in an epoxy monomer based on diglycidyl ether of bisphenol A (DGEBA). In this system, PEO is the miscible block while PE is the crystallizable immiscible block. Initially, the BCP was mixed with DGEBA monomer at 150 °C (*i.e.*, above the melting temperature of PE, that was around 90 °C), and then the mixture was cooled down to room temperature. In this step, long crystalline nanoribbons of several microns in length were obtained in the reactive solvent. To preserve the crystalline structure of these micelles, DGEBA was cured at room temperature by visible-light photopolymerization. Note that in this example, crystallization of the micellar core took place in a medium with high mobility constituted by the liquid solution before polymerization.

A different situation occurs when polymerization is performed above the melting temperature of the crystallizable core-forming block. In this case, crystallization takes place during the final cooling step in a medium whose mobility has been severely reduced by the cure reaction. Puig *et al.*²³ studied the same PE-*b*-PEO/DGEBA system than Zucchi *et al.*,²² but polymerization was performed at 120 °C (above the melting temperature of PE). When

the reaction was completed and the sample was allowed to cool, crystallization of PE took place at 65 °C followed immediately by vitrification of the matrix at 58 °C. Under such conditions, crystallization of PE blocks was confined within individual micelles and a dispersion of short platelets of 23 nm in length was obtained. In this context, it can be inferred that the mobility of the matrix during crystallization of the core-forming block plays a crucial role in the elongation process of these planar structures. We examine this hypothesis in the present contribution.

This work provides an important link with our previous studies on nanostructuring of PE-*b*-PEO block copolymer in epoxy matrices.^{22,23} Here, we demonstrate for the first time that the use of a dual thermal- and photo-curing system allows to regulate the mobility of the matrix during crystallization of PE blocks and, consequently, to generate a dispersion of nanoribbons of precisely controlled length. In addition, we present experimental evidence on the elongation mechanism of 1D nanoribbons. The understanding of the processes taking place during micellar growth is crucial to manipulate the dimensions of the generated nanoribbons with a high level of control.

For this work, PE-*b*-PEO block copolymer was dispersed in DGEBA monomer at a 10 wt% concentration. The mixture was activated with a dual thermal- and photo-curing system, which allowed us to initiate the epoxy polymerization at 120 °C until a certain degree of conversion, stop the reaction by cooling to induce crystallization and micellar elongation, and then continue the polymerization at room temperature by visible-light irradiation. In this way, crystallization of PE blocks took place in a matrix whose mobility was controlled by the degree of conversion reached at 120 °C. By using this protocol, elongated planar nanostructures with controlled length were obtained. Experimental evidence attained from differential scanning calorimetry (DSC), transmission electron microscopy (TEM), and *in situ* small-angle X-ray scattering (SAXS) allowed us to propose a consistent mechanism to describe the formation of these structures. The work demonstrates that the use of a dual thermal- and photo-curing system represents a helpful synthetic tool to generate well-defined 1D nanoribbons in thermosetting matrices.

Experimental section

Materials

The amphiphilic block copolymer used in this study was PE-*b*-PEO ($M_n = 1400$; 50 wt% PEO, Aldrich Chemical Co.). The epoxy monomer was based on diglycidyl ether of bisphenol A (DGEBA, DER 332, Aldrich Chemical Co.) with an epoxy equivalent weight of 174.3 g eq.⁻¹, corresponding to 0.015 hydroxyls per epoxy group. Benzyltrimethylammonium hexafluoroantimonate (Ph₂ISbF₆, Gelest Inc.), camphorquinone (CQ, Aldrich Chemical Co.) and ethyl-4-dimethyl aminobenzoate (EDMAB, Aldrich Chemical Co.) was employed to activate the epoxy system for visible light polymerization. All materials were used as received.

Sample preparation

Samples containing 10 wt% PE-*b*-PEO activated with a dual thermal- and photo-curing system were prepared in the following way. A proper amount of PE-*b*-PEO was blended with one-half of the total mass of DGEBA by stirring at 150 °C. This blend was previously nitrogen purged at room temperature for 30 min to avoid degradation of PEO during blending. Then, the sample was allowed to cool to room temperature and the remaining mass of DGEBA containing 4 wt% Ph₂ISbF₆, 2 wt% CQ and 2 wt% EDMAB, was added. The resulting mixture was nitrogen purged at room temperature for 15 min, and subsequently heated and stirred at 150 °C. After that, the sample was cooled to room temperature and BDMA in a molar ratio with respect to epoxy groups equal to 0.1 was added. Finally, the mixture was again heated to 150 °C, stirred for about 1 min and sandwiched between two glass plates separated by a 1 mm rubber spacer ring used to regulate the sample thickness.

A protocol of two consecutive thermal- and photo-curing steps was employed to polymerize the samples. Thermal curing was carried out at 120 °C in an oven under nitrogen atmosphere. The polymerization was stopped at different conversion degrees by immersing the samples in a cooling bath at −14 °C. After that, samples were allowed to reach room temperature and the second curing step was performed by visible light irradiation using a ring-shaped array of LEDs with a wavelength range between 410–530 nm and an irradiance $I = 140 \text{ mW cm}^{-2}$. The thermal curing step consists of an anionic homopolymerization of epoxy monomers initiated by a tertiary amine (BDMA), while the photocuring step at room temperature takes place *via* a photoinitiated cationic ring-opening polymerization. Both polymerization mechanisms have been extensively discussed in the literature,^{32,33} and are briefly described in the ESI.†

Characterization techniques

Fourier transform infrared spectroscopy (FTIR). Measurements were performed on a Nicolet 6700 Thermo Scientific spectrometer. Data were collected over the range 4000–7000 cm^{-1} from 32 co-added scans at 4 cm^{-1} resolution. To follow the conversion of epoxy groups during the thermal curing step, the device was provided with a heated transmission cell (HT-32, Spectra Tech) and a programmable temperature controller (CAL 9500P, Spectra Tech, $\Delta T \pm 0.1 \text{ }^\circ\text{C}$). For the photocuring step, the sample was irradiated *in situ* with the ring-shaped array of LEDs and spectra were acquired at different exposure times. In both cases, conversion was calculated by measuring the height of the absorption band of epoxy groups at 4530 cm^{-1} with respect to a reference band at 4620 cm^{-1} .^{34,35}

The progress of the glass transition temperature (T_g) of the epoxy system as a function of conversion (x) was calculated by applying the following equation:³⁶

$$(T_g - T_{g0})/(T_{g\infty} - T_{g0}) = \lambda x/[1 - (1 - \lambda)x] \quad (1)$$

where T_{g0} is the glass transition temperature of the unreacted system, $T_{g\infty}$ is the glass transition temperature of the fully reacted network, and $\lambda = \Delta C_{p\infty}/\Delta C_{p0}$ is the ratio of changes in

the isobaric heat capacity through the glass transition for fully polymerized and unreacted systems.

Differential scanning calorimetry (DSC). A PerkinElmer Pyris 1 differential scanning calorimeter was used to determine the thermal transitions that occur during cooling and heating scans. Dry nitrogen was used as the purge gas, and samples of about 10 mg were analyzed. Each sample was held at 120 °C for a certain time, then cooled at 10 °C min^{-1} to −40 °C (cooling scan), and finally heated at 10 °C min^{-1} to 120 °C (heating scan). The glass transition temperature (T_g) was taken at the onset value of the change in the specific heat, the melting temperature (T_m) was defined as the minimum of the endothermic peak, and the crystallization temperature (T_c) was defined as the maximum of the exothermic peak.

Transmission electron microscopy (TEM). Cured samples were microtomed at room temperature using an LKB ultramicrotome equipped with a diamond knife, and ultrathin sections of *ca.* 60 nm in thickness were collected on copper grids. Stained specimens were prepared by exposing the sections to the vapors of a 0.5 wt% aqueous solution of RuO₄ for 15 min. The resulting ultrathin sections were examined with a JEOL 100CX electron microscope operated at 80 kV.

Small-angle X-ray scattering (SAXS). SAXS measurements were conducted in a XEUSS 1.0 HR (XENOCOS, Grenoble) apparatus equipped with a Pilatus 100 K detector (Dectris, Switzerland) and a microfocus X-ray source, using $\lambda = 1.5419 \text{ \AA}$ wavelength radiation. The sample-to-detector distance was determined to be 1354 mm, and an acquisition time of 3 min was used. Cured samples were analyzed at room temperature. For *in situ* experiments, the reaction mixture was placed inside a borosilicate glass capillary with a thickness of 0.01 mm (Hampton Research) and an external diameter of 1.5 mm. The capillary was placed in a holder mounted in the X-ray beam path, and a HFSX350 device (Linkam Scientific Instruments) was used to control the sample temperature within $\pm 0.1 \text{ K}$. The sample was allowed to react at 120 °C until a certain conversion value, and then SAXS data were collected during the cooling step. A SAXS curve was recorded every 10 °C keeping the sample in an isothermal condition during the acquisition time. The SASfit software package was used to analyze scattering profiles.

Results and discussion

The experiments described here examine the possibility of generating a dispersion of elongated planar nanostructures with controllable length by regulating the mobility of the matrix during crystallization of the core-forming block. For this purpose, PE-*b*-PEO block copolymer was dispersed in DGEBA monomer at a 10 wt% concentration. The mixture was activated with a dual thermal- and photo-curing system, which allowed us to initiate the epoxy polymerization at 120 °C until a certain degree of conversion, stop the reaction by cooling to induce crystallization and micellar elongation, and then continue the polymerization at room temperature by visible-light irradiation. The polymerization reaction was monitored by following the decay of the IR

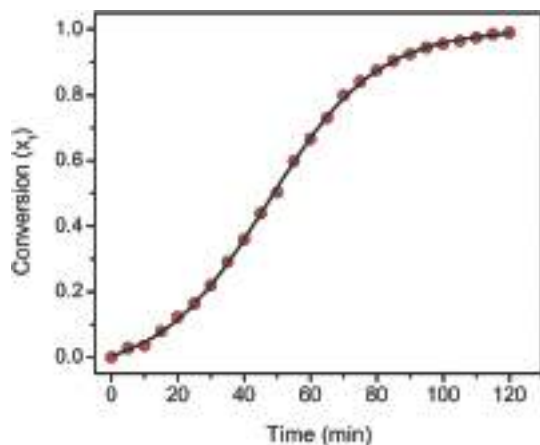


Fig. 1 Conversion of epoxy groups as a function of time for a mixture containing 10 wt% BCP fully polymerized at 120 °C. The black line is drawn to guide the eye.

absorption band of epoxy groups at 4530 cm^{-1} with respect to a reference band at 4620 cm^{-1} .^{34,35} As an example, the conversion (x_t) vs. time curve for a sample fully polymerized at 120 °C is shown in Fig. 1. Throughout the text, x_t is regarded as the epoxy conversion reached during the thermal polymerization step.

Phase behaviour during polymerization at 120 °C

The self-assembly process of the BCP during polymerization of DGEBA at 120 °C has been examined in detail in a previous work and the results are briefly described here (Table 1).²³ The unreacted mixture at 120 °C was macrophase separated as evidenced by the presence of domains with micrometer scale sizes dispersed throughout the sample. These macrodomains consisted of a molten BCP rich phase in the disordered state. Note that the order–disorder transition temperature of the BCP is 111 °C (see Fig. S1 in the ESI[†]), while the melting temperatures of PE and PEO blocks are around 90 and 30 °C, respectively.²² It was also demonstrated by *in situ* SAXS measurements that separated macrodomains coexisted with a population of monodisperse spherical micelles. At 22 min reaction ($x_t = 0.14$), macrodomains were completely disintegrated into spherical micelles as a result of the dissolution of PEO blocks promoted by polymerization. This effect was ascribed to the increment in the concentration of OH groups during ring-opening polymerization of DGEBA, and the formation of hydrogen bonds between these OH groups and the ether groups of PEO. The disintegration

Table 1 Structural parameters of the micellar aggregates formed during polymerization at 120 °C

Reaction time (min)	Conversion (x_t)	Structure
0–22	0–0.14	Macrodomains + spherical micelles ($d_{\text{sph}} = 13\text{ nm}$) ^a
22–52	0.14–0.55	Spherical micelles ($d_{\text{sph}} = 13\text{ nm}$) ^a
68–120	0.77–1	Cylindrical micelles ($d_{\text{cyl}} = 10.5\text{ nm}$; $L_{\text{cyl}} = 23\text{ nm}$) ^b

^a Average diameter of spherical micelles (d_{sph}). ^b Average diameter (d_{cyl}) and length (L_{cyl}) of cylindrical micelles.

of macrodomains was completed prior to gelation of the epoxy matrix, which occurred at 34 min ($x_{\text{gel}} = 0.22$), as determined from rheological measurements. Between 52 min ($x_t = 0.55$) and 68 min reaction ($x_t = 0.77$), a micellar sphere-to-cylinder transformation took place as a result of the tendency of the system to reduce its total free energy. This transformation occurred through a coalescence process, where two spherical micelles merged to form one cylindrical micelle. After this process, the BCP remained self-assembled into cylindrical micelles until the end of the reaction. The structural parameters of the micellar aggregates formed during polymerization at 120 °C are summarized in Table 1.

Crystallization of PE blocks during the cooling step

In the first place, DSC tests were performed to characterize the crystallization behaviour of PE blocks and the glass transition temperature of the epoxy matrix after the thermal polymerization step. Fig. 2a shows the DSC cooling scans recorded after holding each sample at 120 °C until a certain conversion value (x_t), as indicated on each curve. Since the polymerization reaction becomes very slow below 100 °C, we can assume that there were no significant changes in the conversion values during the cooling scans. The unreacted sample ($x_t = 0$) displayed a main crystallization exotherm at a peak temperature of 93 °C. This is the typical crystallization behaviour of heterogeneously nucleated PE in relatively large domains, where crystal growth can propagate over a micrometer scale.³⁷ As can be seen, the main crystallization exotherm gradually shifted to lower temperatures as the matrix conversion increased, indicating that crystallization of PE blocks was confined within progressively smaller domains. The sample fully polymerized at 120 °C ($x_t = 1$) displayed the lowest peak crystallization temperature (61 °C), and thus the higher degree of confinement obtained. This exotherm can be attributed to the crystallization of PE blocks confined within the individual micelles formed during reaction at 120 °C. It can be seen that this crystallization exotherm that peaks at 61 °C was also present in the other samples analyzed, although its enthalpy progressively decreased for lower conversion values. Note that this exotherm, which appears at the maximum supercooling, could be associated with surface nucleation of heterogeneity-free individual micelles.^{38–40} The obtained results suggest that larger structures were formed by aggregation of the micellar units during the cooling step, and that the size of the resulting structures was regulated by the conversion degree of the matrix. We will return to this issue later where we will discuss further evidences for this process.

Fig. 2b shows the DSC subsequent heating scans that were applied to the samples after the cooling scans shown in Fig. 2a. The arrows indicate the glass transition of the epoxy matrix for each sample. The unreacted mixture ($x_t = 0$) displayed the $T_{\text{g,matrix}}$ at -36 °C (onset value) and the melting of PE crystals at 102 °C (minimum of the endothermic peak). In addition, a small melting peak of PEO crystals was detected at 36 °C . As conversion increased, $T_{\text{g,matrix}}$ shifted to higher temperatures due to the increment in molar mass during the pre-gel state and the increase in crosslink density during the post-gel stage. For example, $T_{\text{g,matrix}}$ evolved to -6 °C and 50 °C for conversion

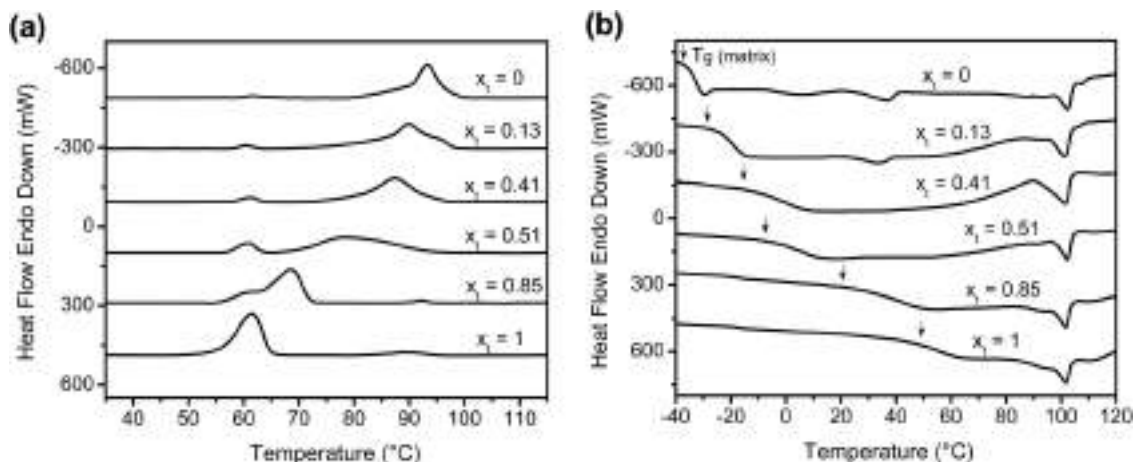


Fig. 2 DSC thermograms at $10\text{ }^{\circ}\text{C min}^{-1}$ for samples containing 10 wt% BCP: (a) cooling scans recorded after holding each sample at $120\text{ }^{\circ}\text{C}$ until a certain conversion value, as indicated on each curve; (b) subsequent heating scans after the cooling shown in (a), for each sample indicated. The arrows indicate the glass transition of the epoxy matrix for each sample.

values of 0.51 and 1 respectively. On the other hand, the values corresponding to the melting peak temperature of PE decreased slightly with increasing conversion, which indicates the presence of progressively smaller PE crystals according to the Gibbs–Thomson effect.⁴¹

Data obtained from DSC scans are summarized in Fig. 3, where the main peak crystallization temperature of PE blocks ($T_{c,PE}$) together with the glass transition temperature of the epoxy matrix ($T_{g,matrix}$) are plotted as a function of conversion. The blue solid line represents the evolution of $T_{g,matrix}$ predicted by eqn (1). Conceptually, this equation is based on entropic considerations applied to a model of the thermosetting polymer consisting of a random mixture of a fully reacted network with the initial monomers in an amount which depends on the particular conversion level.³⁶ This is a valid assumption in this work, since in an anionic epoxy homopolymerization the reacting system consists of epoxy monomers and high-molar-mass polymer at any stage of reaction.⁴² As can be seen, an excellent

fit of the experimental $T_{g,matrix}$ data was obtained, using $\lambda = 0.348$, $T_{g0} = -36\text{ }^{\circ}\text{C}$ and $T_{g\infty} = 50\text{ }^{\circ}\text{C}$.

For a given conversion value, a marked increase in the molecular mobility of the reaction medium occurs as temperature increases above the $T_{g,matrix}$. The term molecular mobility includes different types of motions, such as mass transfer caused by a chemical potential gradient, molecular diffusion reflecting Brownian movements, or rotation of atoms groups or polymeric segments around covalent bonds.⁴³ Therefore, the temperature gap between the crystallization of PE blocks and the glass transition of the matrix ($T_{c,PE} - T_{g,matrix}$) provides a measure of the mobility of the medium during the crystallization process. As can be seen in Fig. 3, this temperature gap can be easily manipulated by adjusting the conversion degree reached during the thermal polymerization step. This method offers us a sophisticated strategy for controlling the length of the micelles that are formed, as shown in the next section.

Characterization of the resulting nanostructures

After the cooling step, the partially polymerized samples were irradiated with visible light at room temperature (*i.e.* below the melting temperature of PE), with the aim of resuming the crosslinking reaction preserving the nanostructures generated during the crystallization process. Under these conditions, the polymerization continued slowly until a vitrification conversion of about 0.9 was reached. The irradiation time depended on the particular conversion degree of each sample. For example, for a sample reacted to a conversion of 0.2 during the thermal curing step ($x_1 = 0.2$), 24 hours of irradiation were required to achieve the vitrification conversion, as shown in Fig. S2 of the ESI.† Note that after photocuring at room temperature, a thermal postcuring treatment at a temperature slightly above $50\text{ }^{\circ}\text{C}$ should be carried out to reach full conversion (see Fig. 3). The postcuring effect is assumed to be due to the activation of the still-alive propagating species when the sample is devitrified. We have verified that the morphology of the generated nanostructures is not modified during such thermal treatment.

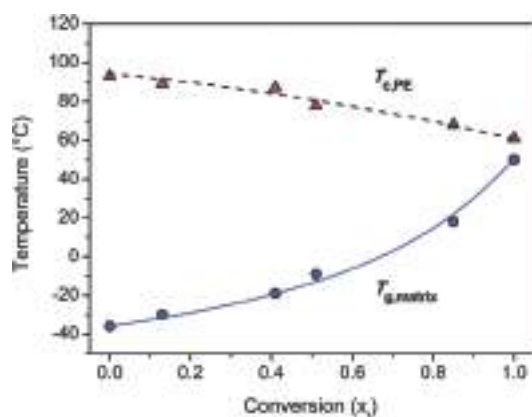


Fig. 3 Main peak crystallization temperature of PE blocks ($T_{c,PE}$, red triangles) and glass transition temperature of the epoxy matrix ($T_{g,matrix}$, blue circles) obtained from DSC scans versus conversion. The blue solid line represents the evolution of $T_{g,matrix}$ predicted by eqn (1), with $\lambda = 0.348$, $T_{g0} = -36\text{ }^{\circ}\text{C}$ and $T_{g\infty} = 50\text{ }^{\circ}\text{C}$. The dashed line was drawn to guide the eye.

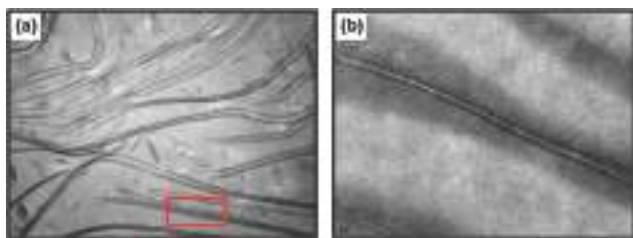


Fig. 4 TEM images of the material obtained without reacting at 120 °C ($x_t = 0$). (a) Unstained image at lower magnification, the black bar represents 200 nm. The red rectangle shows a face-to-face stacking of nanoribbons (see text). (b) Image at higher magnification of a specimen stained with RuO_4 prior to the TEM observation, the black bar represents 10 nm.

The resulting nanostructures after the photopolymerization step were examined by TEM. Fig. 4a shows a selected micrograph of the material obtained without reacting at 120 °C ($x_t = 0$). In this image, since the sectioned specimen was not stained prior to the TEM observation, the contrast is due to the crystalline PE cores.²² As can be seen, very long ribbon-like micelles of about 200 nm in width and several micrometers in length were obtained. An interesting feature of these nanoribbons is their tendency to orient parallel to each other, resulting in face-to-face stacking into lamellar arrangements, such as shown by the red rectangle in Fig. 4a. This behaviour evidences the planar nature of these structures that tend to stack to minimize unfavorable interactions with the matrix.⁴⁴

To further increase the contrast between the phases, a sectioned specimen of the same material ($x_t = 0$) was stained with RuO_4 prior to the TEM observation. Since PEO blocks are preferentially stained by RuO_4 (compared to PE blocks and epoxy matrix), PEO-rich regions look darker in the TEM images.²² A high-magnification micrograph is shown in Fig. 4b. Here, it is observed a micelle viewed edge-on with PE blocks forming the core (lighter line) and PEO blocks forming the corona (darker lines). From this image,

we estimate that the thickness of the PE core is *ca.* 6 nm. Since each methylene group contributes with 0.1253 nm to the chain length,⁴⁵ and the PE block has 50 methylene units, we deduce that extended PE crystals must have a length of 6.27 nm, which is in agreement with the core thickness estimated from the TEM image. Therefore, it is inferred that crystals are formed by interdigitated PE chains, with PEO blocks protruding from the planar interfaces in an alternating way.

TEM images of the materials obtained with different conversion degrees reached during the thermal polymerization step are shown in Fig. 5. For comparison purposes, the images are shown at the same magnification. Note that the sectioned specimens were stained with RuO_4 prior to the TEM observation. As can be seen, the average length of the micelles decreased progressively as x_t increased. For the particular case of the material fully polymerized at 120 °C ($x_t = 1$), the mean micelle length was only 26 nm (Table 2). It can be observed that small micellar units of between 15 and 30 nm in length were also present in the other samples analyzed, even for $x_t = 0$ (see Fig. S3 in the ESI†). As shown previously, the PE blocks self-assembled into these individual micelles exhibited the lowest crystallization temperature (61 °C) as a consequence of the extreme degree of confinement (see Fig. 2a).

Histograms of the micelle lengths were calculated by TEM image analysis (Fig. 6). For each material, more than 100 micelles were traced by hand to determine their length using the Image-Pro Plus software. The corresponding values of number-average length (L_n), weight-average length (L_w), and length dispersity (L_w/L_n) are listed in Table 2. For reference, the temperature gap between $T_{c,PE}$ and $T_{g,matrix}$ has been included for each value of x_t (Table 2). The results confirm that the average length of the micelles decreases as the difference between $T_{c,PE}$ and $T_{g,matrix}$ decreases, which is a consequence of the loss of mobility of the medium during the crystallization process. The dimensions obtained by TEM analysis were consistent with the visual appearance of the samples. Fig. 5 (insets) shows photographs of the prepared materials. As

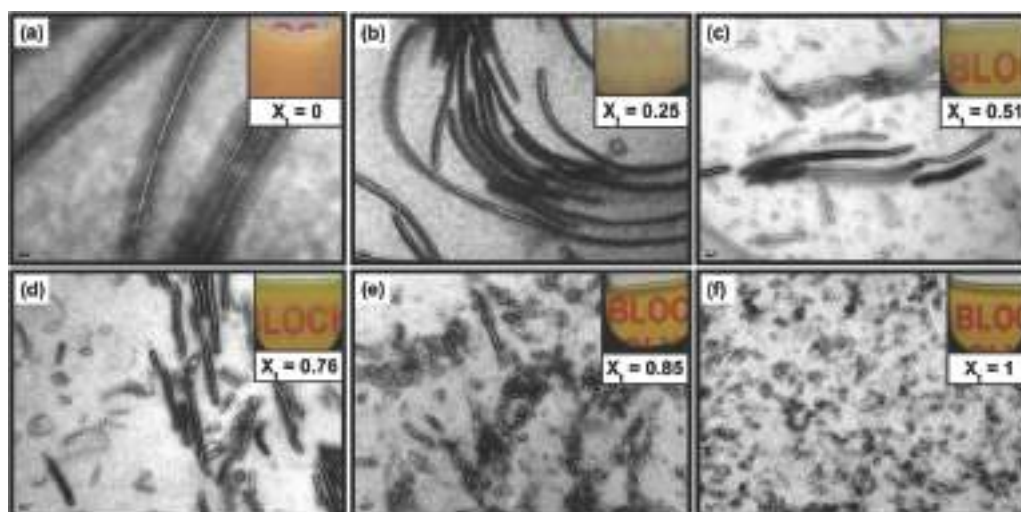


Fig. 5 TEM images of materials obtained with different conversion degrees reached during the thermal polymerization step (x_t). Sectioned specimens were stained with RuO_4 prior to the TEM observations. In all the images, the scale bar represents 20 nm. The insets show photographs of the corresponding materials. (a) $x_t = 0$; (b) $x_t = 0.25$; (c) $x_t = 0.51$; (d) $x_t = 0.76$; (e) $x_t = 0.85$; and (f) $x_t = 1$.

Table 2 Average lengths of micelles and temperature gap between the crystallization of PE blocks and the glass transition of the matrix, for the different samples

Sample (x_t)	L_n (nm)	L_w (nm)	L_w/L_n	$T_{c,PE}-T_{g,matrix}$ (°C)
0	1837	2838	1.54	129
0.25	527	776	1.47	114
0.51	243	366	1.50	92
0.76	230	411	1.79	62
0.85	38	46	1.21	47
1	26	28	1.06	11

can be seen, the fully photocured sample ($x_t = 0$) was opaque due to the presence of ribbon-like micelles with lengths at the micron scale (Fig. 5a). With increasing x_t , there was a gradual decrease in opacity, indicating that the size of the micelles progressively decreased below the wavelength of visible light (Fig. 5b–d). For $x_t = 0.85$ and 1, the samples were fully transparent as expected for a dispersion of nanoscale objects (Fig. 5e and f). In each case, the micelle length distribution was properly described by a log-normal distribution, which is represented by the black solid line in Fig. 6a–f.

Structural information of the ribbon-like micelles was also obtained from SAXS analysis, which provides more reliable information from the statistical point of view. Scattering intensity curves corresponding to samples obtained with different values of x_t are shown in Fig. 7a. For $x_t = 0$, the magnitude of the slope in the low- q region was equal to 2.1, indicating the existence of elongated planar nano-objects.⁴⁶ As can be seen, the magnitude of the slope at small q gradually decreased with increasing x_t , which denotes a decrease in the size of the scattering objects.

These results are consistent with the evidence obtained from TEM analysis. As mentioned above, the long ribbon-like micelles have a tendency to orient parallel to each other, resulting in face-to-face stacking into lamellar arrangements (see Fig. 4a). Additional evidence for this feature was revealed by SAXS data. For example, for $x_t = 0$ it can be observed the presence of a principal maximum of spatial correlation at $q^* = 0.24 \text{ nm}^{-1}$ along with a secondary maximum located at $2q^*$. Such a sequence is characteristic of a lamellar arrangement of planar objects with an average lamellar period of 26.2 nm ($2\pi/q^*$). Correlation maxima can also be distinguished in the SAXS curves corresponding to $x_t = 0.25, 0.51$ and 0.76 . For samples with shorter micelles ($x_t = 0.85$ and 1), the lamellar structure is no longer discerned, which reveals the absence of face-to-face stacking in these materials. This assertion is also supported by TEM images (see Fig. 5e and f).

SAXS data were analyzed using the SASfit software package, in the q range between 0.08 and 0.5 nm^{-1} where structural information of ribbon-like micelles is contained. In all cases, the form factor was modeled with the HomogeneousXS algorithm, assuming the presence of elongated planar objects with a log-normal length distribution. In each instance, the best fit to SAXS data led to a thickness for planar objects of around 8 nm. In order to account for the correlation maxima observed for $x_t = 0, 0.25, 0.51$ and 0.76 , a lamellar structure factor (paracrystalline model) was added in these cases, with an average stacking separation of about 25 nm. A brief description of the models used and the best-fitting parameters is presented in the ESI† (Table S1). As shown in Fig. 7b, a very good fitting of SAXS data was achieved. In the next section, we use these models to analyze

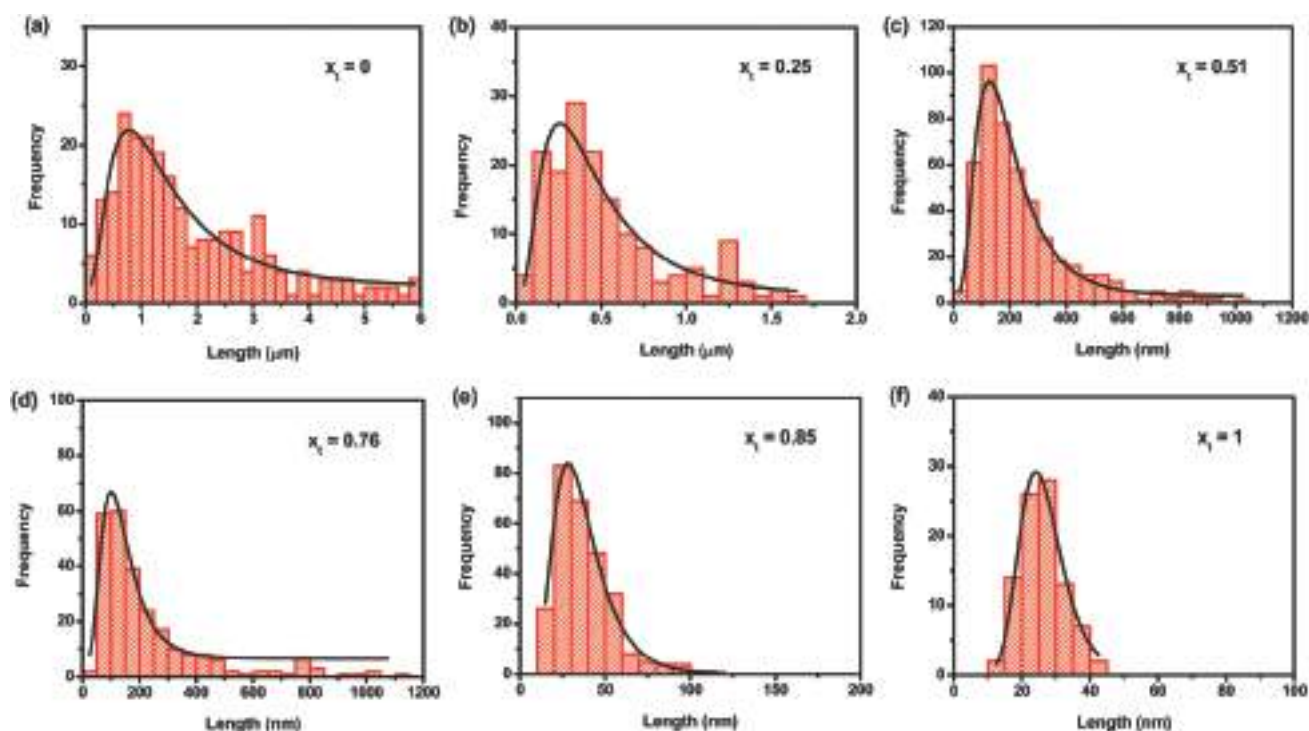


Fig. 6 Histograms of the micelle lengths for materials prepared with different conversion degrees reached during the thermal polymerization step (x_t). The black solid lines represent the fitting curves with log-normal distributions. (a) $x_t = 0$; (b) $x_t = 0.25$; (c) $x_t = 0.51$; (d) $x_t = 0.76$; (e) $x_t = 0.85$; and (f) $x_t = 1$.

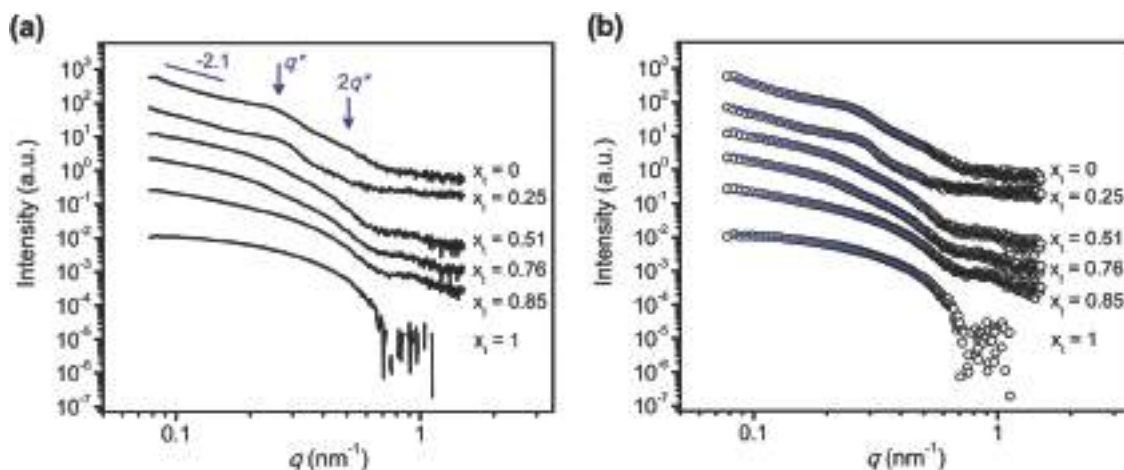


Fig. 7 (a) SAXS curves of samples prepared with different conversion degrees reached during the thermal polymerization step (x_t). The curves were vertically displaced for clarity. (b) Fitting of SAXS data shown in (a), in the q range between 0.08 and 0.5 nm^{-1} .

in situ SAXS data with the aim of unravelling the elongation mechanism of ribbon-like micelles.

Growth mechanism of ribbon-like micelles

To investigate the mechanism of micellar growth, *in situ* SAXS experiments were performed. For this, the reaction mixture was placed in a holder mounted in the X-ray beam path, and allowed to react at 120 °C until a certain value of x_t . Then, SAXS data were collected during the cooling step. Fig. 8a shows scattering intensity curves obtained at different temperatures for $x_t = 0.3$. Data obtained at 120 °C were modeled assuming the presence of polydisperse spherical micelles with an average diameter of 9.8 nm, which is in good agreement with the results previously reported.²³ The analysis of SAXS data obtained at 90, 70 and 50 °C required to assume the presence of elongated planar objects with a log-normal length distribution, and a lamellar structure factor. This means that the elongation process took place at 90 °C. Within the uncertainty to compare temperatures obtained in different devices, this agrees with the crystallization temperature of PE blocks for the same value of x_t (see Fig. 3).

On the other hand, Fig. 8b shows SAXS curves recorded during the cooling step for a sample with $x_t = 0.7$. In this case, data obtained at 120 and 90 °C were analyzed assuming polydisperse spherical micelles ($d_{\text{sph}} = 12$ nm) and a mixture of polydisperse spherical and cylindrical micelles ($d_{\text{sph}} = 12$ nm; $d_{\text{cyl}} = 12$ nm; $L_{\text{cyl}} = 46$ nm), respectively; while data obtained at 70 and 50 °C required to assume elongated planar objects with a log-normal length distribution, and a lamellar structure factor. Therefore, in contrast to the previous case, the micellar elongation process was detected at 70 °C, in agreement with the crystallization temperature of PE blocks for $x_t = 0.7$. In view of these results, we can infer that crystallization and micellar elongation proceed concomitantly, rather than step-wise as reported for ribbon-like poly(styrene-*block*- ϵ -caprolactone) (PS-*b*-PCL) micelles dispersed in a PS matrix.²⁴

These findings lead us to rationalize the elongation mechanism of ribbon-like micelles as a diffusion-limited colloid aggregation process which is induced by crystallization of PE cores. During reaction at 120 °C, the block copolymer is self-assembled into spherical or short cylindrical micelles depending on the

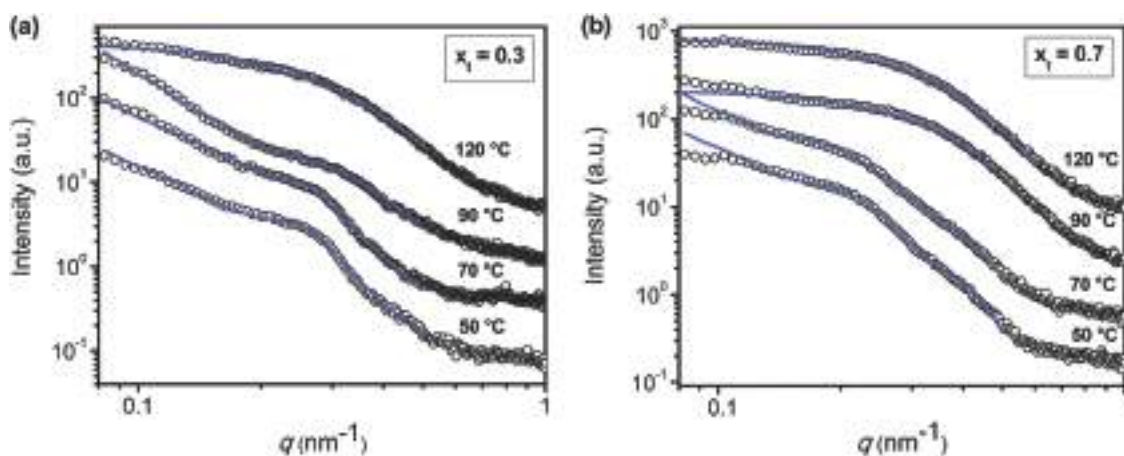


Fig. 8 Fitting of SAXS curves recorded *in situ* during the cooling step for samples with: (a) $x_t = 0.3$; and (b) $x_t = 0.7$. The curves were vertically displaced for clarity.

conversion degree (x_t). At this stage, micellar units themselves are colloidally stable as long as the PE core remains molten. As temperature decreases during the cooling step, individual micelles become colloidally unstable and tend to aggregate. The driving force towards aggregation comes from the tendency of PE blocks to crystallize with high enthalpy gain.⁴⁴ Because PE crystallizes very rapidly,⁴⁷ the aggregation rate will be limited by diffusion, that is to say, by the time taken for micelles to encounter each other. Lin *et al.*⁴⁸ demonstrated that the aggregation process of colloidal systems under diffusion-limited aggregation conditions is universal, independent of the detailed chemical nature of the colloids. Under this circumstance, the size of the aggregates formed during the cooling step will decrease as the mobility of the medium, and therefore the diffusivity of particles, decrease. The aggregation process is immediately followed by crystallization of PE cores. The temperature at which crystallization develops depends on the aggregate size. In this way, we explain why PE blocks confined within smaller aggregates crystallized at lower temperatures. This idea is consistent with that of Chen *et al.*,⁴⁹ who demonstrated through experiments at fixed cooling rate that the crystallization temperature in nano-scaled microdomains of a block copolymer system can be precisely tailored by the microdomain morphology. They argued that such correlation between morphology and crystallization temperature can be associated with the frustration of crystal growth caused by the nanoscopically limited continuity of microdomains. Note that when crystal growth can propagate over the micron scale (for $x_t = 0$ and 0.25), PE blocks crystallize at a temperature comparable to that of spherulitic crystallization in homopolymer. The fact that the structures are elongated and remain thin suggests that the preferential crystal growth direction is that of the long axis of the semicrystalline core, with a slower growth in width, and with negligible growth in perpendicular direction to the planar faces. This assertion is supported by the evidence that crystals are formed by interdigitated PE chains, with PEO blocks protruding from the planar interfaces and acting as a barrier to growth in this direction.

There is another feature of the formation process of ribbon-like micelles that must be considered. For x_t values in the range between 0 and 0.14, the BCP is macrophase separated at 120 °C forming micrometer-size domains (with the block copolymer in a disordered molten state), that coexist with spherical micelles (see Table 1). During the cooling step, a series of events take place within these macrodomains. First, the BCP self-organizes into a lamellar structure at its order–disorder transition temperature (111 °C). This process is followed by crystallization of PE blocks at around 95 °C. Meanwhile, the miscibility of PEO blocks with epoxy increases, since they exhibit a lower critical solution temperature (LCST) type behaviour.⁵⁰ Finally, dissolution of PEO blocks in epoxy promotes the dispersion of individual elongated planar nano-objects (nanoribbons) constituted of a crystallized PE core bordered by PEO segments, the same configuration as that obtained by the diffusion-limited colloid aggregation mechanism. Since the length of these nanoribbons is typically in the micrometer range, the dispersion process can be clearly observed by transmission optical microscopy (TOM),

as shown in the ESI† (Fig. S4). Nanoribbons obtained for $x_t = 0$ were mostly generated through this mechanism. Here, the high mobility of the medium played a crucial role in dispersing nanoribbons throughout the epoxy system.

Conclusions

Crystallization-driven self-assembly of PE-*b*-PEO block copolymer was used to generate a dispersion of core-crystalline nanoribbons in an epoxy matrix. We demonstrated that the length of the ribbon-like nanostructures can be controlled by regulating the mobility of the epoxy matrix during crystallization of the core-forming PE block. This was achieved by activating the initial mixture with a dual thermal- and photo-curing system, which allowed us to initiate the epoxy polymerization at 120 °C until a certain degree of conversion, stop the reaction by cooling to induce crystallization and micellar elongation, and then continue the polymerization at room temperature by visible-light irradiation. The mechanism of micellar growth was conceptualized as a diffusion-limited colloid aggregation process which was induced by crystallization of PE cores. During reaction at 120 °C, the BCP was self-assembled into spherical or short cylindrical micelles depending on the conversion degree. As temperature decreased during the cooling step, individual micelles became colloidally unstable and tended to aggregate driven by the propensity of PE blocks to crystallize with a high enthalpy gain. Under diffusion-limited aggregation conditions, the size of the aggregates formed during the cooling step decreased as the mobility of the medium, and therefore the diffusivity of particles, decreased. The aggregation process was immediately followed by crystallization of PE cores. For each sample analyzed, the temperature difference between the crystallization of PE blocks and the glass transition of the matrix was determined as a way to evaluate the mobility of the medium during the crystallization process. It was found that the average length of the micelles decreased progressively from 1.8 μm to 26 nm as the difference between $T_{c,PE}$ and $T_{g,matrix}$ decreased from 129 to 11 °C, respectively. The novel approach delivered in this contribution represents a powerful route to 1D planar nanostructures with precisely controlled dimensions. The methodology may, in principle, be applicable to any amphiphilic block copolymer with a core-forming block that crystallizes easily.

Author contributions

The manuscript was written through contributions of all authors. All authors have given approval to the final version of the manuscript.

Conflicts of interest

There are no conflicts to declare.

Acknowledgements

The financial support of the following institutions is gratefully acknowledged: National Research Council (CONICET, Argentina),

National Agency for the Promotion of Science and Technology (ANPCyT, Argentina), and University of Mar del Plata. R. N. S. thanks Comisión de Investigaciones Científicas (CIC) de la Provincia de Buenos Aires (Argentina) for a doctoral fellowship.

References

- 1 X. Li, X. Wang, L. Zhang, S. Lee and H. Dai, *Science*, 2008, **319**, 1229–1232.
- 2 J. Cai, P. Ruffieux, R. Jaafar, M. Bieri, T. Braun, S. Blankenburg, M. Muoth, A. P. Seitsonen, M. Saleh, X. Feng, K. Müllen and R. Fasel, *Nature*, 2010, **466**, 470–473.
- 3 P. Masih Das, G. Danda, A. Cupo, W. M. Parkin, L. Liang, N. Kharche, X. Ling, S. Huang, M. S. Dresselhaus, V. Meunier and M. Drndić, *ACS Nano*, 2016, **10**, 5687–5695.
- 4 B. Radisavljevic, A. Radenovic, J. Brivio, V. Giacometti and A. Kis, *Nat. Nanotechnol.*, 2011, **6**, 147–150.
- 5 Z. Wang, K. Zhao, H. Li, Z. Liu, Z. Shi, J. Lu, K. Suenaga, S.-K. Joung, T. Okazaki, Z. Jin, Z. Gu, Z. Gao and S. Iijima, *J. Mater. Chem.*, 2010, **21**, 171–180.
- 6 A. Isogai, T. Saito and H. Fukuzumi, *Nanoscale*, 2011, **3**, 71–85.
- 7 J. M. Moreno, I. Navarro, U. Díaz, J. Primo and A. Corma, *Angew. Chem., Int. Ed.*, 2016, **55**, 11026–11030.
- 8 S. Iijima, T. Yumura and Z. Liu, *Proc. Natl. Acad. Sci. U. S. A.*, 2016, **113**, 11759–11764.
- 9 M. Yagmurcukardes, F. M. Peeters, R. T. Senger and H. Sahin, *Appl. Phys. Rev.*, 2016, **3**, 041302.
- 10 J. Bang, U. Jeong, D. Y. Ryu, T. P. Russell and C. J. Hawker, *Adv. Mater.*, 2009, **21**, 4769–4792.
- 11 J. Wu, Y. S. Thio and F. S. Bates, *J. Polym. Sci., Part B: Polym. Phys.*, 2005, **43**, 1950–1965.
- 12 J. J. Crassous, P. Schurtenberger, M. Ballauff and A. M. Mihut, *Polymer*, 2015, **62**, A1–A13.
- 13 L. Shen, H. Wang, G. Guerin, C. Wu, I. Manners and M. A. Winnik, *Macromolecules*, 2008, **41**, 4380–4389.
- 14 X. Wang, G. Guerin, H. Wang, Y. Wang, I. Manners and M. A. Winnik, *Science*, 2007, **317**, 644–647.
- 15 G. Guerin, G. Cambridge, M. Soleimani, S. Mastour Tehrani, I. Manners and M. A. Winnik, *J. Phys. Chem. B*, 2014, **118**, 10740–10749.
- 16 L. Cao, I. Manners and M. A. Winnik, *Macromolecules*, 2002, **35**, 8258–8260.
- 17 C. E. Boott, E. M. Leitao, D. W. Hayward, R. F. Laine, P. Mahou, G. Guerin, M. A. Winnik, R. M. Richardson, C. F. Kaminski, G. R. Whittell and I. Manners, *ACS Nano*, 2018, **12**, 8920–8933.
- 18 G. Guerin, P. A. Rugar, I. Manners and M. A. Winnik, *Nat. Commun.*, 2018, **9**, 1158.
- 19 A. M. Mihut, M. Drechsler, M. Möller and M. Ballauff, *Macromol. Rapid Commun.*, 2010, **31**, 449–453.
- 20 W.-N. He, B. Zhou, J.-T. Xu, B.-Y. Du and Z.-Q. Fan, *Macromolecules*, 2012, **45**, 9768–9778.
- 21 L. Yin, T. P. Lodge and M. A. Hillmyer, *Macromolecules*, 2012, **45**, 9460–9467.
- 22 I. A. Zucchi and W. F. Schroeder, *Polymer*, 2015, **56**, 300–308.
- 23 J. Puig, I. A. Zucchi, M. Ceolín, W. F. Schroeder and R. J. J. Williams, *RSC Adv.*, 2016, **6**, 34903–34912.
- 24 Ú. M. Montoya Rojo, C. C. Riccardi, M. D. Ninago, A. E. Ciolino, M. A. Villar, M. Ceolín, I. A. Zucchi and W. F. Schroeder, *Eur. Polym. J.*, 2019, **112**, 704–713.
- 25 P. M. Lipic, F. S. Bates and M. A. Hillmyer, *J. Am. Chem. Soc.*, 1998, **120**, 8963–8970.
- 26 F. Meng, S. Zheng, H. Li, Q. Liang and T. Liu, *Macromolecules*, 2006, **39**, 5072–5080.
- 27 H. E. Romeo, I. A. Zucchi, M. Rico, C. E. Hoppe and R. J. J. Williams, *Macromolecules*, 2013, **46**, 4854–4861.
- 28 A. B. Leonardi, I. A. Zucchi and R. J. J. Williams, *Eur. Polym. J.*, 2015, **71**, 164–170.
- 29 J. Puig, M. Ceolín, R. J. J. Williams, W. F. Schroeder and I. A. Zucchi, *Soft Matter*, 2017, **13**, 7341–7351.
- 30 S. Xu, C. Zhang, L. Li and S. Zheng, *Polymer*, 2017, **128**, 1–11.
- 31 C. Zhang, L. Li and S. Zheng, *Macromolecules*, 2013, **46**, 2740–2753.
- 32 I. E. Dell’Erba and R. J. J. Williams, *Polym. Eng. Sci.*, 2006, **46**, 351–359.
- 33 I. E. dell’Erba, F. D. Martínez, C. E. Hoppe, G. E. Elicabe, M. Ceolín, I. A. Zucchi and W. F. Schroeder, *Langmuir*, 2017, **33**, 10248–10258.
- 34 N. Poisson, G. Lachenal and H. Sautereau, *Vib. Spectrosc.*, 1996, **12**, 237–247.
- 35 B.-G. Min, Z. H. Stachurski, J. H. Hodgkin and G. R. Heath, *Polymer*, 1993, **34**, 3620–3627.
- 36 J. P. Pascault and R. J. J. Williams, *J. Polym. Sci., Part B: Polym. Phys.*, 1990, **28**, 85–95.
- 37 M. T. Casas, R. M. Michell, I. Blaszczyk-Lezak, J. Puiggali, C. Mijangos, A. T. Lorenzo and A. J. Müller, *Polymer*, 2015, **70**, 282–289.
- 38 A. T. Lorenzo, M. L. Arnal, A. J. Müller, A. Boschetti-de-Fierro and V. Abetz, *Macromolecules*, 2007, **40**, 5023–5037.
- 39 R. M. Michell, I. Blaszczyk-Lezak, C. Mijangos and A. J. Müller, *Polymer*, 2013, **54**, 4059–4077.
- 40 R. M. Michell and A. J. Müller, *Prog. Polym. Sci.*, 2016, **54–55**, 183–213.
- 41 M. Perez, *Scr. Mater.*, 2005, **52**, 709–712.
- 42 J.-P. Pascault, H. Sautereau, J. Verdu and R. J. J. Williams, *Thermosetting Polymers*, CRC Press, 2002.
- 43 A. Hale, C. W. Macosko and H. E. Bair, *Macromolecules*, 1991, **24**, 2610–2621.
- 44 D. Richter, D. Schneiders, M. Monkenbusch, L. Willner, L. J. Fetters, J. S. Huang, M. Lin, K. Mortensen and B. Farago, *Macromolecules*, 1997, **30**, 1053–1068.
- 45 A. N. Parikh, S. D. Gillmor, J. D. Beers, K. M. Beardmore, R. W. Cutts and B. I. Swanson, *J. Phys. Chem. B*, 1999, **103**, 2850–2861.
- 46 O. Glatter and O. Kratky, *Small Angle X-ray Scattering*, Academic Press, 1982.
- 47 R. P. Patki and P. J. Phillips, *Eur. Polym. J.*, 2008, **44**, 534–541.
- 48 M. Y. Lin, H. M. Lindsay, D. A. Weitz, R. C. Ball, R. Klein and P. Meakin, *Nature*, 1989, **339**, 360.
- 49 H.-L. Chen, S.-C. Hsiao, T.-L. Lin, K. Yamauchi, H. Hasegawa and T. Hashimoto, *Macromolecules*, 2001, **34**, 671–674.
- 50 A. B. Leonardi, I. A. Zucchi and R. J. J. Williams, *Eur. Polym. J.*, 2015, **65**, 202–208.